High-resolution multi-z confocal microscopy with a diffractive optical element

BINGYING ZHAO,[1,*] 🆔 **MINORU KOYAMA,**[2] 🆔 **AND JEROME MERTZ**[3] 🆔

[1]*Department of Electrical and Computer Engineering, Boston University, 44 Cummington Mall, Boston, MA 02215, USA*

[2] *Department of Cell and Systems Biology, University of Toronto, 1265 Military Trail, Scarborough, ON M1C1A4, Canada*

[3]*Department of Biomedical Engineering, Boston University, 44 Cummington Mall, Boston, MA 02215, USA*

*byzhao@bu.edu

Abstract: There has been recent interest in the development of fluorescence microscopes that provide high-speed volumetric imaging for life-science applications. For example, multi-z confocal microscopy enables simultaneous optically-sectioned imaging at multiple depths over relatively large fields of view. However, to date, multi-z microscopy has been hampered by limited spatial resolution owing to its initial design. Here we present a variant of multi-z microscopy that recovers the full spatial resolution of a conventional confocal microscope while retaining the simplicity and ease of use of our initial design. By introducing a diffractive optical element in the illumination path of our microscope, we engineer the excitation beam into multiple tightly focused spots that are conjugated to axially distributed confocal pinholes. We discuss the performance of this multi-z microscope in terms of resolution and detectability and demonstrate its versatility by performing *in-vivo* imaging of beating cardiomyocytes in engineered heart tissues and neuronal activity in *c. elegans* and zebrafish brains.

1.   Introduction

Microscopy systems that image multicellular environments over large three-dimensional (3D) fields of view (FOVs) with high spatiotemporal resolution have become increasingly important in the fields of life science [1]. Several approaches for fast volumetric imaging have been developed over the past two decades to address this need [2].

One class of volumetric imaging approaches is based on the use of widefield microscopy, which benefits from the capability of modern cameras to rapidly provide images with massive pixel counts. Volumetric imaging with high spatiotemporal resolution can be achieved by fast z-axis scanning [3–6], or alternatively by recording multiple focal planes simultaneously with several cameras [7–9], or by focus splitting with a single camera using a diffractive optical element [10–12], a specialized beamsplitter [13–15], or light-field detection [16–18]. However, as is common with widefield microscopy, these approaches do not inherently provide optical sectioning and are thus susceptible to the out-of-focus background, which can degrade image contrast and SNR. Such image degradation can be mitigated by numerical post-processing [19–23]. Alternatively, temporally coded light-sheet array microscopy [24] and point spread function engineering with multiplane light-sheet microscopy [25] can provide parallelized 3D imaging with improved depth resolution. However, background reduction remains compromised when imaging in thick tissue owing to scattered light impinging on the camera sensor, which limits the use of these techniques to weakly scattering or optically cleared tissues or sparsely labeled samples.

Another class of volumetric imaging approaches is based on the use of laser scanning microscopy (LSM), which includes confocal and multiphoton microscopy. These methods provide better optical sectioning and image contrast by the physical rejection of out-of-focus background or

by nonlinear excitation. Quasi-volumetric imaging can be achieved with nonlinear SLM by extending the excitation focus, for example, with the use of a Bessel beam [26,27]. Alternatively, quasi-instantaneous multiplane imaging can be achieved by spatiotemporal multiplexing of the excitation focus [28,29]; however, this approach is technically complicated. We previously showed that confocal microscopy can also be parallelized to achieve multiplane imaging with the use of multiple detection foci, as opposed to multiple excitation foci, which we called multi-z confocal microscopy. In point scanning geometries, the multiple detection foci can be produced by multiple reflecting pinholes [30,31]. In line scanning geometries, they can be produced by reflecting slits [32] or by rolling-shutter gating [14] (the former provides improved detection efficiency per plane). Our implementations of multi-z microscopy were based on the use of an extended excitation focus produced by underfilling the objective back aperture to achieve low-NA illumination. While simple, this strategy leads to reduced spatial resolution, both lateral and axial, compared to conventional confocal microscopy. In some cases, such as when performing ultrafast imaging with low signal strengths [31], a reduced spatial resolution can be advantageous. In other cases, however, a reduced resolution can be a drawback. A strategy to improve axial resolution can involve angularly offsetting the illumination and detection foci [14], akin to confocal theta microscopy [33]. Here, we present an alternative approach to improve the resolution of multi-z microscopy, both laterally and axially, by engineering the illumination point spread function (PSF) with a diffractive optical element (DOE).

A basic principle of multi-z confocal microscopy is to detect signals from multiple focal planes simultaneously by using multiple axially distributed detection pinholes conjugated to each plane. In this manner, the first pinhole efficiently collects signal from the deepest plane, the second pinhole efficiently collects signal from the next deepest plane, and so forth. Fluorescence signals can be simultaneously generated at each plane with the use of an extended low-NA excitation focus. Bearing in mind that lateral and axial resolution scale as NA^{-1} and NA^{-2} respectively, such low-NA excitation leads to overall compromised resolution and prescribes the use of relatively large pinholes for efficient signal collection. The key novelty in our current implementation of multi-z microscopy is that we replace our single-focus low-NA excitation beam with a multi-focus high-NA excitation beam. To do this, we use a custom-made DOE specifically designed to split the illumination into multiple (here 4) foci of roughly equal power, axially aligned to be conjugate to the multiple detection pinholes (also 4). Because the excitation foci are produced using the full objective aperture, they are spatially much more confined than in our previous single-focus implementation, allowing the use of smaller pinholes and significantly increasing resolution both in the lateral and axial dimensions. We characterize the performance of our new multi-focus implementation of multi-z microscopy in terms of both resolution and detectability. We also demonstrate the capabilities of our microscope by performing near video-rate imaging of beating sarcomeres in engineered cardiac micro tissues and hearts in zebrafish, and *in-vivo* calcium dynamics in *c. elegans* and zebrafish.

## 2. High-resolution multi-z implementation

2.1. Microscope design

Our microscope configuration is shown in Fig. 1(b). Briefly, it is similar to conventional confocal microscopy but with variants in both the excitation and the detection optics. We use a diode laser (Omicron LuxX+ 488 nm, 200 mW) as the excitation source. A custom-made DOE (HOLO-OR MF-005-R-Y-A) shapes the beam into four foci distributed along the propagation axis with an average inter-focus distance ($\triangle Z_{DOE}$) of 1007 μm (Fig. 1(a)). A galvo-resonant scanner (Thorlabs 8 kHz, SK-GR08/M) provides video-rate XY-scanning. The laser beam is expanded and relayed to overfill the back pupil plane of the objective (Nikon CFI LWD Plan Fluorite Water 16×, 0.8NA) to achieve high-NA illumination. Denoting by M_{exc} the net de-magnification from the foci produced by the DOE to the foci within the sample, the inter-focus separation within the

sample ($\triangle Z_{sample}$) is thus given by

$$\triangle Z_{sample} = nM_{exc}^2 \triangle Z_{DOE} \tag{1}$$

where n is the sample refractive index. In our case $M_{exc} = 0.12$, leading to simultaneous 4-plane illumination with $\triangle Z_{sample} \approx 20\mu m$.
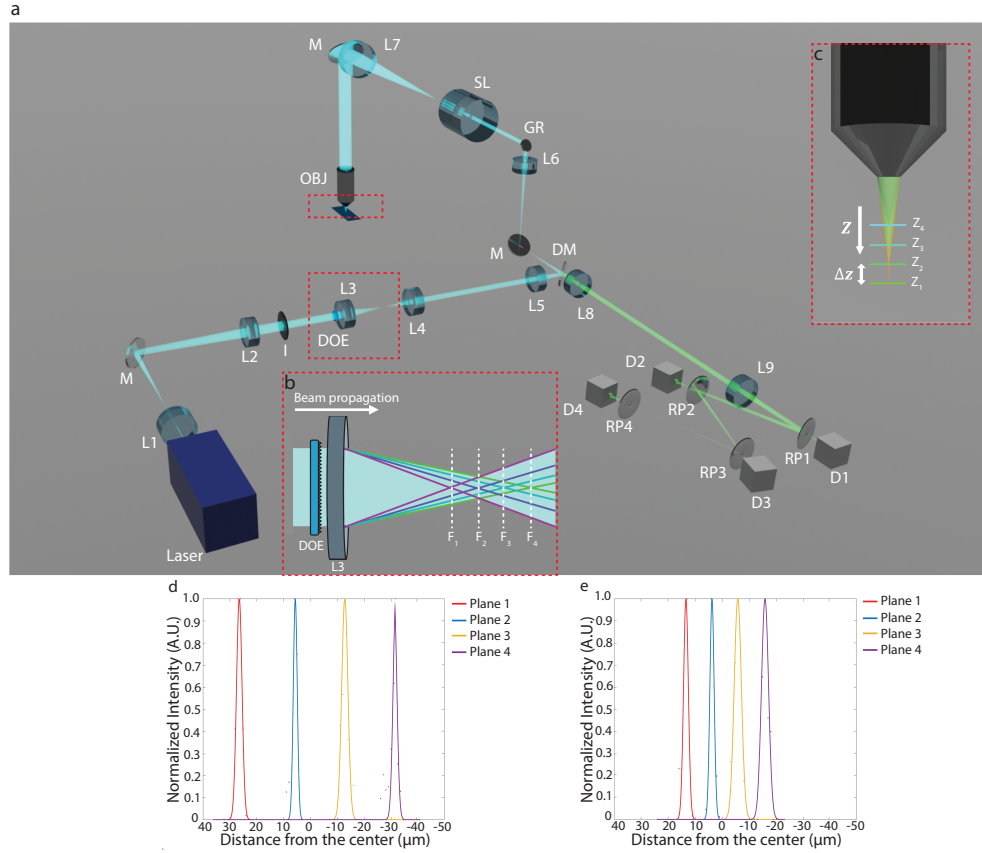
Fig. 1. (a) Schematic of multi-z microscope, with expanded views of (b) multiple foci (here 4) produced by DOE and (c) resultant multiple foci delivered into sample. L: lens, M: mirror, DM: dichromatic mirror, SL: scan lens, GR: galvo-resonant scanners, RP: reflective pinhole, D: detector. Detailed information about components is provided in Supplement 1. Normalized intensity produced by a fluorescent bead when axially scanned through the imaging planes with (d) a 16× objective ($f_{obj} = 12.5$mm), and (e) a 20× objective ($f_{obj} = 9$mm). Planes 1-4: deepest to shallowest.

The detection optics is essentially the same as in [30] but with smaller pinholes and a different inter-pinhole separation. The generated fluorescence signal is epi-detected through the same high-NA objective and de-scanned by the same galvo-resonant scanner. The fluorescence signal is routed by a dichromatic mirror (Semrock Di01-R488/561) and relayed onto a set of four reflective pinholes (National Aperture 214-0556 - 150um Round Aperture), axially distributed so as to be conjugate to the four excitation foci. The distance between the reflective pinholes ($\triangle Z_{pinhole}$) is dependent on the magnification M_{det} from the object space in the sample to the image space at the detectors, and is given by

$$\triangle Z_{pinhole} = \frac{1}{n}M_{det}^2\triangle Z_{sample} = M_{det}^2 M_{exc}^2 \triangle Z_{DOE} \tag{2}$$

where in our case $M_{det} = 85.71$, leading to $\triangle Z_{pinhole} \approx 110$mm.

Four separate SiPM detectors (Hamamatsu S14420-1550MG) with homebuilt preamplifiers (same as in [31]) are used to simultaneously record the in-focus fluorescence signals transmitted through the pinholes. The microscope control is performed by Matlab with ScanImage software [34] and a National Instruments interface (NI PXIe-1073).

2.2.   Inter-plane separation adjustment

The use of a fixed DOE in our microscope leads to the constraint that $\triangle Z_{DOE}$ is fixed. In turn, this prescribes a fixed separation between pinholes as determined by Eq. (2). At first glance, it might appear that the inter-plane separation within the sample $\triangle Z_{sample}$ must also be fixed, however this is not quite true. The inter-plane separation can be readily adjusted by swapping in different objectives into our microscope with different focal lengths. This follows from Eq. (1) and the fact that M_{exc}, which is given by

$$M_{exc} = \frac{f_{obj}}{f_{L7}} \times \frac{f_{SL}}{f_{L6}} \times \frac{f_{L5}}{f_{L4}} \tag{3}$$

scales directly with f_{obj}. It is important to note that changing $\triangle Z_{sample}$ does not require us to change $\triangle Z_{pinhole}$. Indeed, from

$$M_{det} = \frac{f_{L7}}{f_{obj}} \times \frac{f_{L6}}{f_{SL}} \times \frac{f_{L9}}{f_{L8}} \tag{4}$$

we find that the total magnification from DOE to pinhole is given by

$$M_{det} M_{exc} = \frac{f_{L9}}{f_{L8}} \times \frac{f_{L5}}{f_{L4}} \tag{5}$$

This total magnification is independent of f_{obj}. It is also independent of the immersion index n. In other words, the microscope pinholes need only be aligned once upon construction, according to Eqs. (2) and (5). Once aligned, the positioning of the pinholes remains invariant and is independent of changes in objective or immersion medium, and hence changes in $\triangle Z_{sample}$.

To demonstrate the flexibility of our microscope, we first imaged an isolated $0.2 \, \mu$m bead (Phosphorex, Fluorophorex Polystyrene Microspheres) over a $90 \, \mu$m axial range using the $16\times$ objective ($f_{obj} = 12.5$mm). The signals recorded from the same bead by the four detection channels reveal that the imaging planes are axially separated by about $20 \, \mu$m (Fig. 1(d)). We then used a $20\times$ objective (Olympus XLUMPLFLN Water $20\times$, 0.9NA, $f_{obj} = 9$mm) to image the same bead without any other modifications made to the microscope. The signals from the same bead revealed that the axial separation between the imaging planes was reduced to about $10 \, \mu$m, as expected (Fig. 1(e) and Fig. S1 and Visualization 5).

2.3.   Resolution and detectability

To evaluate the resolution of our microscope, we imaged isolated $0.2 \, \mu$m fluorescent beads over a $200 \, \mu$m axial range, using the $16\times$ objective. Based on the full-width half maximum of the measured intensities, the average transverse resolution of the four planes was found to be $\delta x = 0.50 \mu$m and the average axial resolution was found to be $\delta z = 3.6 \mu$m (Fig. 2(a)). The lateral and axial resolution for each plane is shown in Fig. S2. The lateral resolution was roughly the same for each detection channel. However, since the principal focal plane of the objective is closer to the second plane, spherical aberration results in a somewhat degraded axial resolution in other planes (Fig. S2(d)). Such 3D resolution is comparable to that obtained with conventional confocal microscopy and is easily adequate for resolving transverse structures on the micron scale.
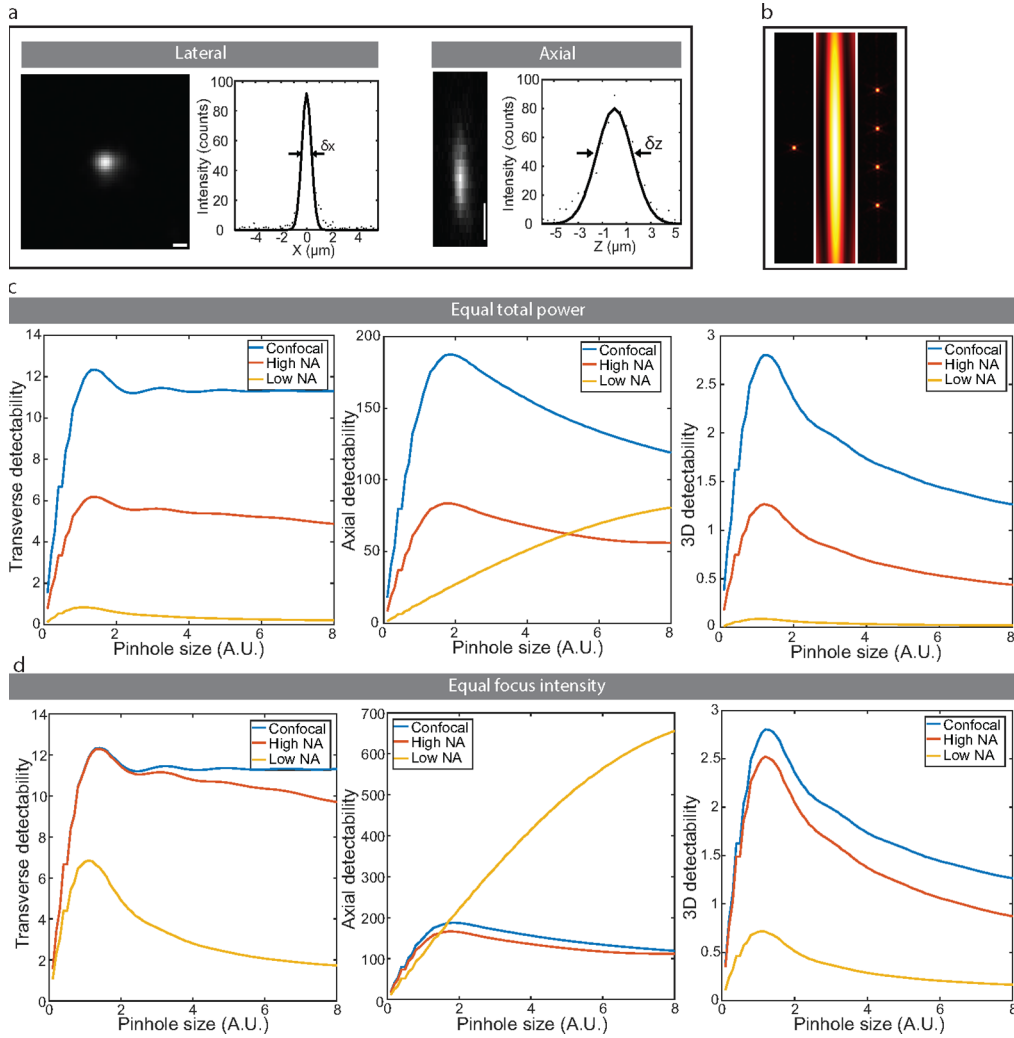
Fig. 2. Resolution and detectability. (a) Average lateral and axial resolution of the four planes as measured with $0.2\,\mu m$ fluorescent bead. Scale bars: horizontal: $0.5\,\mu m$, vertical: $5\,\mu m$ (b) Schematic of excitation beams for conventional confocal, low-NA single-focus, and high-NA multi-focus multi-z microscopy. Comparisons of theoretical detectabilities in cases of (c) equal power and (d) equal focus intensity delivered to the sample. Left: transverse detectability. Middle: axial detectability. Right: 3D detectability.

Another important metric characterizing the performance of a confocal microscope is detectability, which characterizes its ability to detect a fluorescent object in the presence of shot noise produced by background (auto)fluorescence [35,36]. Detectability comes in three variants: transverse (D_v) assesses the ability to detect a point object within a planar background; axial (D_u) assesses the ability to detect a planar object within a volume background; 3D (D_{3D}) assesses the ability to detect a point object within a volume background. These are given by

$$D_v = \frac{PSF_{conf}(0)}{\sqrt{\iint_{\boldsymbol{\rho}} PSF_{conf}(\boldsymbol{\rho}, 0)d\boldsymbol{\rho}}} \tag{6}$$

$$D_u = \frac{\iint_{\boldsymbol{\rho}} PSF_{conf}(\boldsymbol{\rho}, 0) d\boldsymbol{\rho}}{\sqrt{\int_z \iint_{\boldsymbol{\rho}} PSF_{conf}(\boldsymbol{\rho}, z) d\boldsymbol{\rho} dz}} \tag{7}$$

$$D_{3D} = \frac{PSF_{conf}(0)}{\sqrt{\int_z \iint_{\boldsymbol{\rho}} PSF_{conf}(\boldsymbol{\rho}, z) d\boldsymbol{\rho} dz}} \tag{8}$$

We theoretically evaluated these detectabilities for both our previous low-NA single-focus multi-z microscope with 0.1-NA illumination and our present high-NA multi-focus multi-z microscope (same 16× objective), and compared these with conventional confocal microscopy. The excitation beams of the three microscopes are shown in Fig. 2(b). The excitation and emission wavelengths are 488 nm and 510 nm respectively, and the refractive index of the sample is set to 1.33.

In the case of equal powers delivered to the sample (Fig. 2(c)) it is apparent that, while the detectability of our new multi-focus multi-z is significantly improved compared to that of our previous single-focus multi-z, it still falls short of the detectability of a conventional confocal microscope. The reason for this is clear. While the full power of the excitation beam is delivered to the focus of a conventional confocal microscope, only a fraction of the power is delivered to each focus (here about a quarter) in multi-focus multi-z microscopy, leading to reduced signal per focus. On the other hand, if one re-evaluates detectability for the case of equal focus intensities (Fig. 2(d)), one finds that the detectability of our multi-focus multi-z recovers to almost the same level as a conventional confocal microscope. The remaining small discrepancy comes from crosstalk between our microscope's axially distributed foci which somewhat reduces contrast. That is, even though the four foci in our system are as tightly focused as in a conventional confocal microscope, each detection channel can collect a small fraction of the fluorescence generated from different foci. Finally, we note, that the optimal pinhole size for our multi-focus multi-z is roughly the same as that for a conventional confocal microscope, as expected.

3. Methods

3.1. Cardiac micro tissue preparation and imaging

Cardiac micro tissues (CMT) were prepared as described in [37]. In brief, human-induced pluripotent stem cells (hiPSCs) derived from the PGP1 donor from the Personal Genome Project with an endogenous green fluorescent protein (GFP) tag on the sarcomere gene TTN [38] were maintained in mTeSR1 (StemCell) on Natrigel (Fisher) mixed 1:80 in DMEM/F-12 (Fisher). hiPSCs were differentiated into hiPSC-CMs by small-molecule, monolayer-based manipulation of the Wnt signaling pathway [39]. Once the cells were beating, hiPSC-derived cardiomyocytes (CMs) were purified using RPMI no-glucose (Sigma). Selected cells were maintained in RPMI with 1:50 B-27 Supplement (Fisher) on 10 μg/mL fibronectin (Fisher)-coated plates for over 30 days. hiPSC-CMs and Normal Human Ventricular Cardiac Fibroblasts (NHCF-V) were mixed in 7.5 μL ECM solution, 4 mg/mL human fibrinogen (Sigma), 10% Matrigel (Corning), 1.6 mg/mL thrombin (Sigma), 5 μL Y-27632 (Tocris), and 33 μg/mL aprotinin (Sigma). The cell-ECM mixtures were pipetted into the CMT scaffolds [40]. After polymerization for 5 min, growth media containing high-glucose DMEM (Fisher) supplemented with 10% fetal bovine serum (Sigma), 1% GlutaMAX (Fisher), 5 μM Y-27632 (Tocris), and 33 μg/mL aprotinin (Sigma) was added and replaced every other day. Y-27632 was removed two days after seeding. hiPSC-CMTs were imaged on day 7 after seeding. For imaging, the growth media was removed, and PBS was added. Samples were imaged in PBS solution at room temperature using the 16× Nikon objective with an inter-plane separation of 20 μm. An average laser power of 6 mW post objective was used.

3.2.　*C. elegans* preparation and imaging

A transgenic *Caenorhabditis elegans* (*C. elegans*) strain QW1217 (zfIs124[Prgef-1::GCaMP6s]; otIs355[Prab-3::NLS::tagRFP]) that expresses cytoplasmic GCaMP6s was maintained at 20°C on nematode growth medium (NGM)-agarose plates coated with *Escherichia coli* as a food source, and imaged on day 3 after subculturing. 20 μL 2% agarose (Sigma) was coated on a 25 mm ×25 mm region of a glass slide and let sit at 4 °C for 5 min. *C. elegans* of length about 1 mm were selected and immobilized on the agarose pad with several drops of a mixture medium of 5 mM Tetramisole and S-Basal. After the *C. elegans* were immobilized, a coverslip was three-sided sealed above, and several drops of the S-Basal were pipetted into the open side of the coverslip to fill the cavity. Samples were imaged with the 20× Olympus objective with an inter-plane separation of 10 μm. An average post-objective laser power of 2 mW was used.

3.3.　Zebrafish preparation and imaging

For the *in-vivo* structural imaging of zebrafish, transgenic zebrafish embryos (isl2b:Gal4 UAS:Dendra) expressing GFP were maintained in filtered water from an aquarium at 28.5 °C on a 14 - 10 hr light-dark cycle. Zebrafish larvae at 7 days post-fertilization (dpf) were used for imaging. The larvae were embedded in 5% low-melting-point agarose (Sigma) in a 55 mm petri dish. After agarose solidification, the petri dish was filled with filtered water from the aquarium. Samples were imaged with the 16× Nikon objective with an inter-plane separation of 20 μm. An average post-objective laser power of 6 mW was used.

For the in vivo calcium imaging of zebrafish brain, transgenic zebrafish larvae (elavl3:H2B-GCaMP6f) expressing nuclear pan-neuronal GCaMP6f at 6 dpf were used for imaging. Before imaging, the zebrafish larvae were first selected using a stereo fluorescence microscope. Selected zebrafish larvae were embedded in 2% low-melting-point agarose. Samples were imaged with the 16× Nikon objective with an inter-plane separation of 20 μm. An average post-objective laser power of 15 mW was used.

3.4.　Image processing and analysis

For CMT imaging, we manually selected resolved sarcomere band structures in each detection channel using ImageJ. Data analysis was carried out using custom scripts in Matlab. The sarcomere bandwidth was measured as the peak-to-peak separation.

For *c. elegans* imaging, we used the Moco plugin [41] in ImageJ for motion correction and manually selected neurons that expressed spontaneous activity during the imaging session. Calcium activity traces were extracted using a custom Matlab script. $\triangle F/F_0$ was calculated as $\triangle F/F_0 = (F(t) - F_0)/F_0$, where F_0 was the average of the local spatiotemporal background. A Matlab detrend function with linear fitting was applied to correct for photobleaching.

For zebrafish heartbeat imaging, we measured the heart diameter variations as a function of time for the deeper two planes (planes 1 and 2), and intensity variations as a function of time for the shallower two planes (planes 3 and 4). The power spectral density obtained by Fourier transformation was used to characterize heartbeat rate.

For zebrafish calcium imaging, we used a similar method as described in [32]. We used the Moco plugin for motion correction in ImageJ. Afterward, we used a constrained non-negative matrix factorization (CNMF) algorithm [42] in Matlab for neuron identification. $\triangle F/F_0$ was calculated as $\triangle F/F_0 = (F(t) - F_0)/F_0$. Finally, we used a customized Matlab script to select neurons that expressed activity during the imaging session with $\triangle F/F_0$ over 35%.

4. Results

4.1. Dynamic sarcomere imaging in engineered cardiac tissue

Volumetric imaging and quantitative analysis of beating CMTs are essential for the understanding of cell development and function in heart tissue [43], but remain challenging owing to difficulties in monitoring fast motion at sub-micron scales [44].

To demonstrate how high-resolution multi-z microscopy can address this challenge, we performed sarcomere imaging in spontaneously beating hiSPC-CMTs over a $154 \times 154 \times 60 \, \mu m^3$ volume at 5 Hz for a duration of 10 s (see Visualization 1). Sarcomere band structures were resolvable in all four imaging planes (Fig. 3(a)). We observed that the orientation and periodicity of the recorded sarcomere bands were irregular, as expected. We selected a region of interest
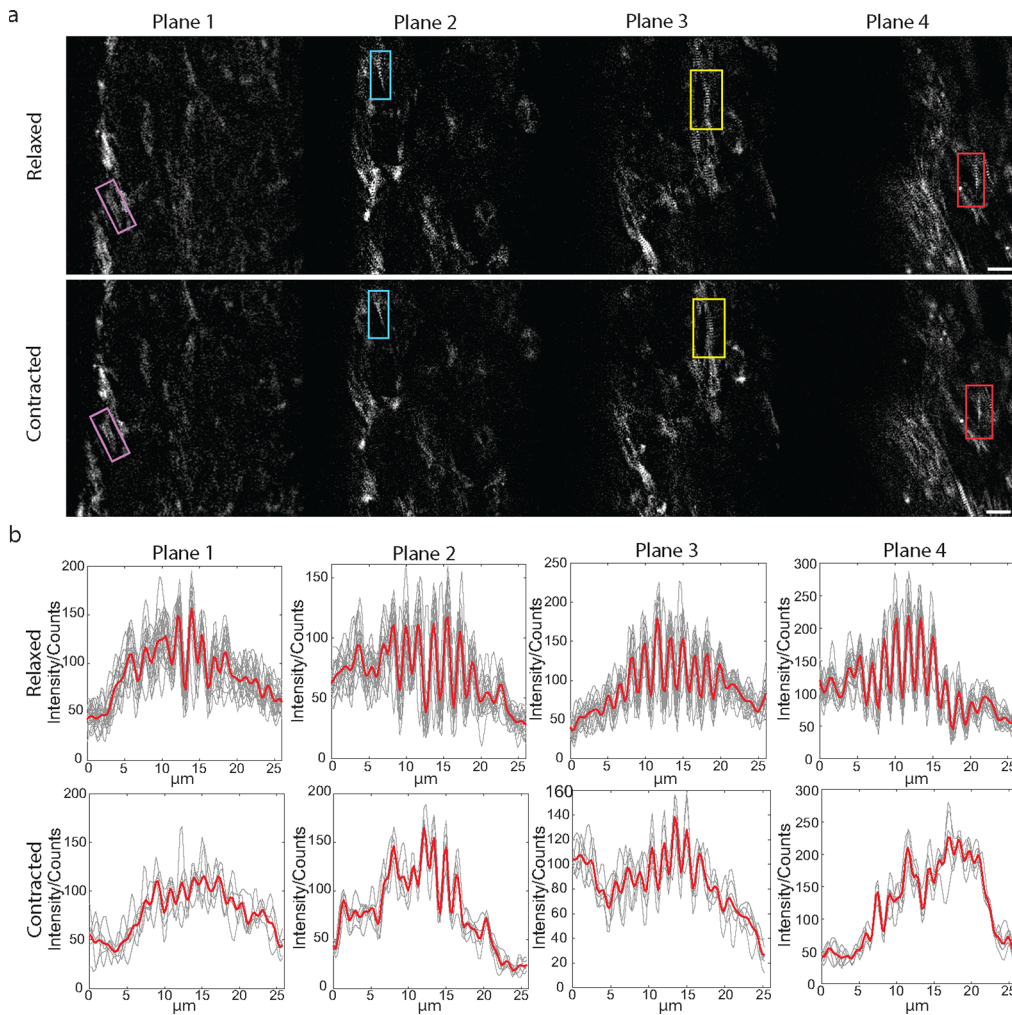
Fig. 3. *In-vitro* imaging of beating engineered cardiac micro tissue. (a) Simultaneous 4-plane images of sarcomeres recorded at two phases of a beat cycle: (top) relaxed, (bottom) contracted. (b) Corresponding intensity plots across sarcomere structures in dashed windows: magenta in plane 1, cyan in plane 2, yellow in plane 3, and red in plane 4. Planes 1-4: deepest to shallowest. Gray traces: superposed plots from each frame. Red traces: mean intensity plots. Scale bar: 15 μm

(ROI) per imaging plane to characterize the sarcomere structure deformation during beating (Fig. 3(b)). When relaxed, the sarcomere band periods were 1.74 μm, 1.66 μm, 1.63 μm, and 1.68 μm in the four planes, from the deepest to the shallowest. When beating, the sarcomere band periods contracted to 1.45 μm, 1.39 μm, 1.51 μm, and 1.38 μm. The sarcomere band structures became shortened by about 85.5% during cardiac tissue beating, providing a measure of sarcomere muscle function.

### 4.2. In-vivo calcium imaging in c. elegans

Understanding the coordinated function of neural circuits is a fundamental goal in neuroscience and a motivation for the development of microscopes capable of performing high-speed volumetric imaging. To demonstrate the capability of our microscope to simultaneously record multiple planes with high optical sectioning capacity, we performed *in-vivo* calcium imaging in *c. elegans*.

An entire *c. elegans* expressing cytoplasmic GCaMP6s, was imaged across three planes separated by $10\mu m$, within a volume of $563 \times 563 \times 20\,\mu m^3$ at 15 Hz for a duration of 4 min
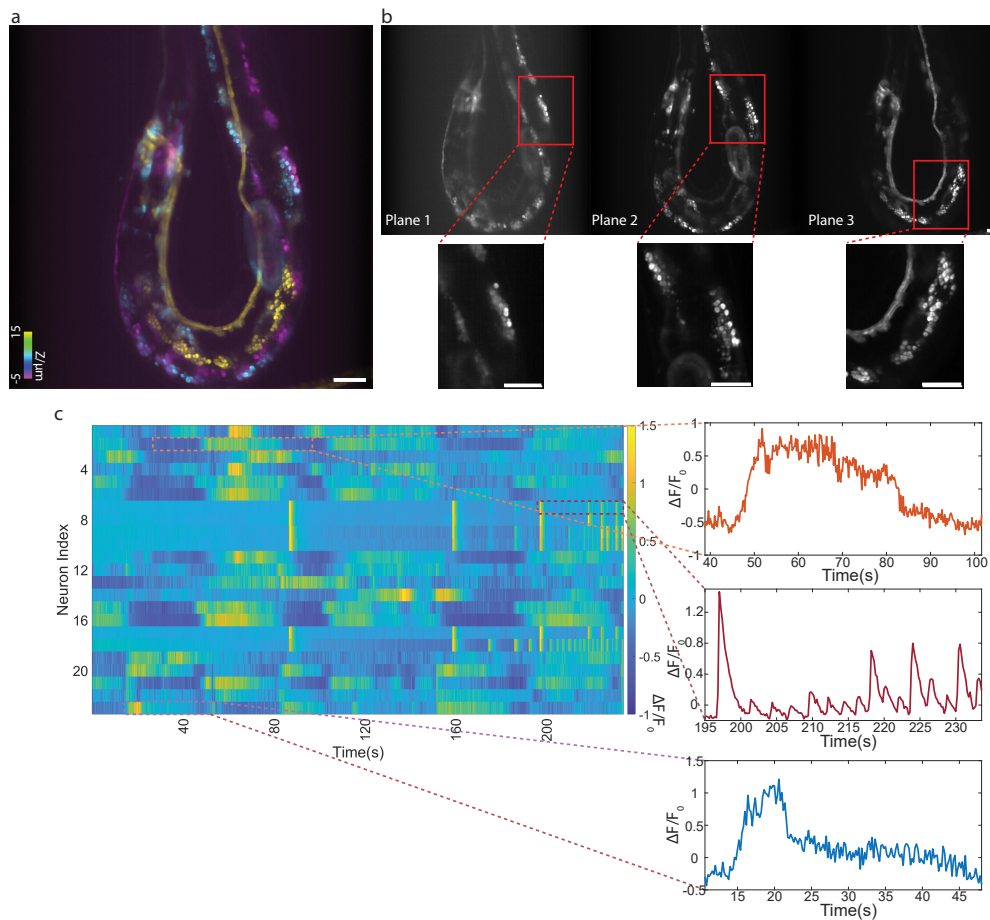
Fig. 4. *In-vivo* calcium imaging of *c. elegans*. (a) Merged temporal max-min projection from three detection planes. (b) Temporal max-min projection from individual planes, with an expanded view of neurons recorded at different depths. Planes 1-3: deepest to shallowest. (c) The activity of 22 distinct neurons identified throughout imaging volume and calcium traces of selected neurons. Scale bar: 50 μm
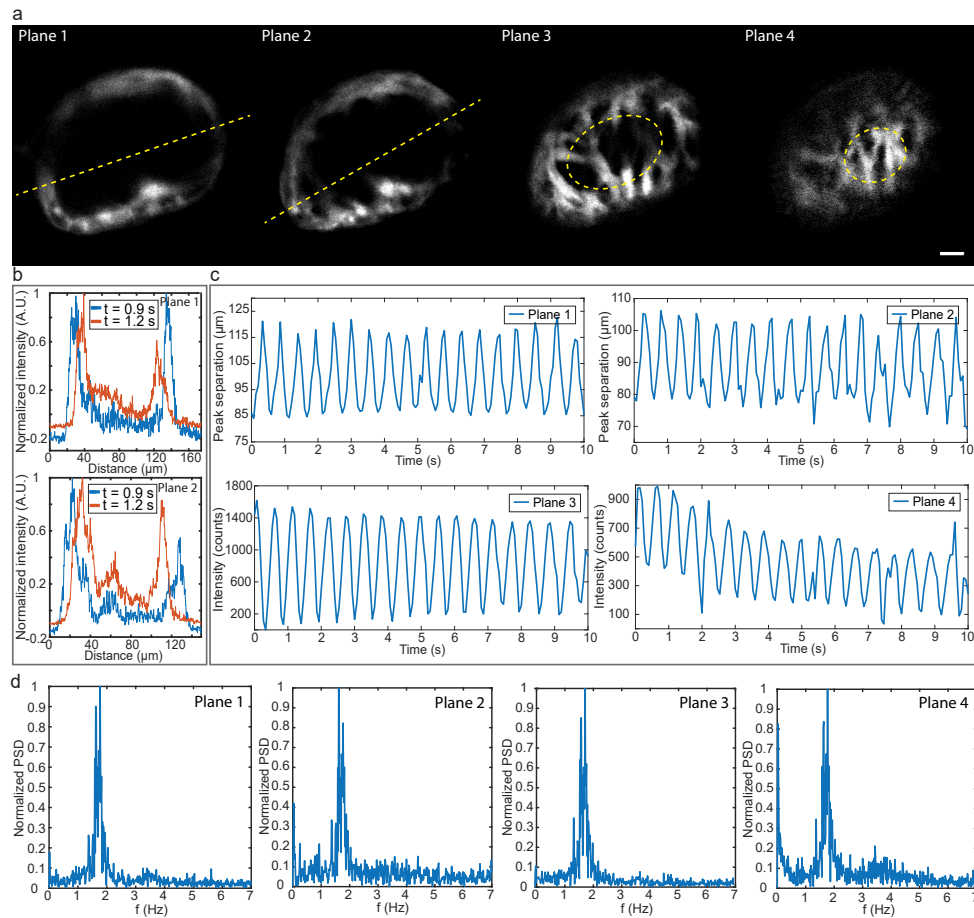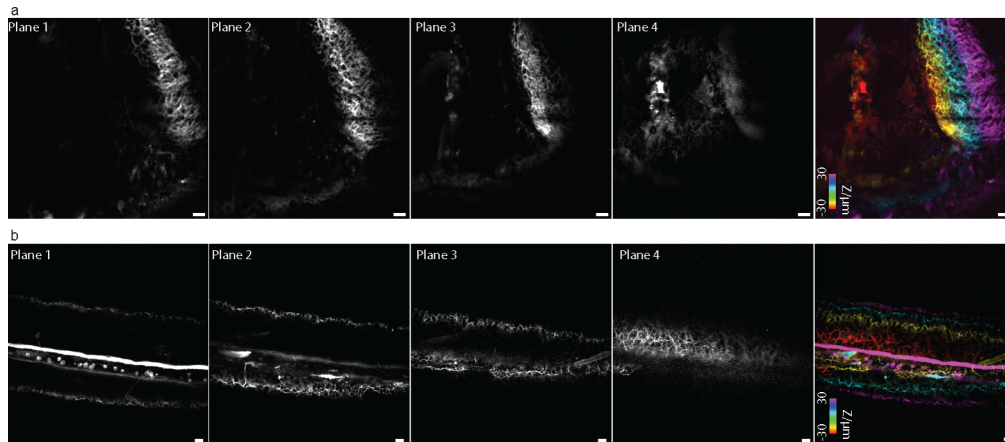
Fig. 5. Zebrafish heart imaging. (a) Single 4-plane image, with planes separated by 20 μm. (b) Intensity plots along yellow lines in (a) at times separated by 0.3 s. Top: plane 1. Bottom: Plane 2. (c) Heartbeat as measured by diameter variations (planes 1 and 2) or intensity variations within elliptical ROIs shown in (a) (planes 3 and 4). (d) Heartbeat power spectral density for each plane. Planes 1-4: deepest to shallowest. Scale bar: 15 μm.

(Visualization 2). Figures 4(a,b) are the temporal max-min projections in each plane. The merged image (Fig. 4(a)) reveals no overlap between planes, and individual neurons are easily resolvable. We manually identified 22 neurons that were active during the imaging session throughout the imaging volume. Temporal $\triangle F/F_0$ traces associated with these neurons are shown in Fig. 4(c). Note that a baby *c. elegans* is clearly visible, whose neuronal activity could be distinguished from that of the mother c. elegans (see Visualization 2 and Fig. S3), illustrating the capacity of our microscope to provide optical sectioning and sub-cellular resolution across multiple depths.

4.3. In-vivo structural imaging in zebrafish

The zebrafish is a commonly used model for the study of developmental biology and neuronal network activity that offers several advantages for imaging, such as relatively clear tissue and relatively small brain size. To further demonstrate the versatility of our multi-z microscope, we performed zebrafish imaging *in vivo*.

Fig. 6. Zebrafish neuronal processes imaging. (a) Brain region. (b) Tail region. Left: single 4-plane image. Right: merged with color corresponding to depth. Planes 1-4: deepest to shallowest. Scale bar: 15 μm.

To begin, we imaged a zebrafish heart (7 dpf) with four planes separated by 20μm, within a volume of $154 \times 154 \times 60 \, \mu\mathrm{m}^3$ at 15 Hz for a duration of 1 min (Visualization 3). Figure 5(a) shows a single 4-plane image, and Fig. 5(b) shows an intensity plot across the heart images recorded in planes 1 and 2 at different times. The peak separations in this plot are used to infer the heart diameter as a function of time (Fig. 5(c)). We also monitored the intensity variations in the ROIs shown for planes 3 and 4 (Fig. 5(c)). The power spectral density of the diameter and intensity variations are shown in Fig. 5(d), from which we inferred the heartbeat rate obtained from each plane, which is consistent though phase shifted between planes. The heartbeat rate was found to be approximately 1.7 Hz.

To highlight the 3D resolution capability of our microscope, we imaged neuronal processes in different regions of the zebrafish. In both dense regions such as the brain (Fig. 6(a)), and sparse regions such as the tail (Fig. 6(b)), our microscope was easily able to resolve individual neurons and axons with high contrast.

4.4. In-vivo calcium imaging in zebrafish brain

We next applied our microscope to *in-vivo* calcium imaging in the zebrafish brain to demonstrate its capacity to provide fast, functional imaging over extended volumes.

We imaged the entire brain of a zebrafish (6 dpf) that expressed nuclear GCaMP6f, with four planes separated by 20μm, within a volume of $768 \times 384 \times 60 \, \mu m^3$ at 15 Hz for a duration of 5 min (Visualization 4). Figure 7(a) shows the temporal max-min projection for the merged four channels. Using CNMF, we selected 141, 213, 216, and 204 neurons from the four planes (deepest to shallowest). No crosstalk is observed between planes owing to the high axial resolution and the 20 μm inter-plane separation. The identified neurons and temporal $\triangle F/F_0$ traces obtained from each plane are shown in Fig. S4. Figures 7(b), (c), and (d) show zoomed-in views of the brainstem, optic tectum-cerebellum, and telencephalon in Fig. 7(a). In the brainstem, we selected 13, 16, 22, and 16 neurons from each plane; in the optic tectum-cerebellum, we selected 9, 12, 15, and 21 neurons; in the telencephalon, we selected 99, 123, 123, and 73 neurons, from deepest to shallowest. Note that the number of resolved neurons in each plane is greater than the selected neurons shown in Fig. 7 because not all neurons expressed spontaneous activity during the imaging session.
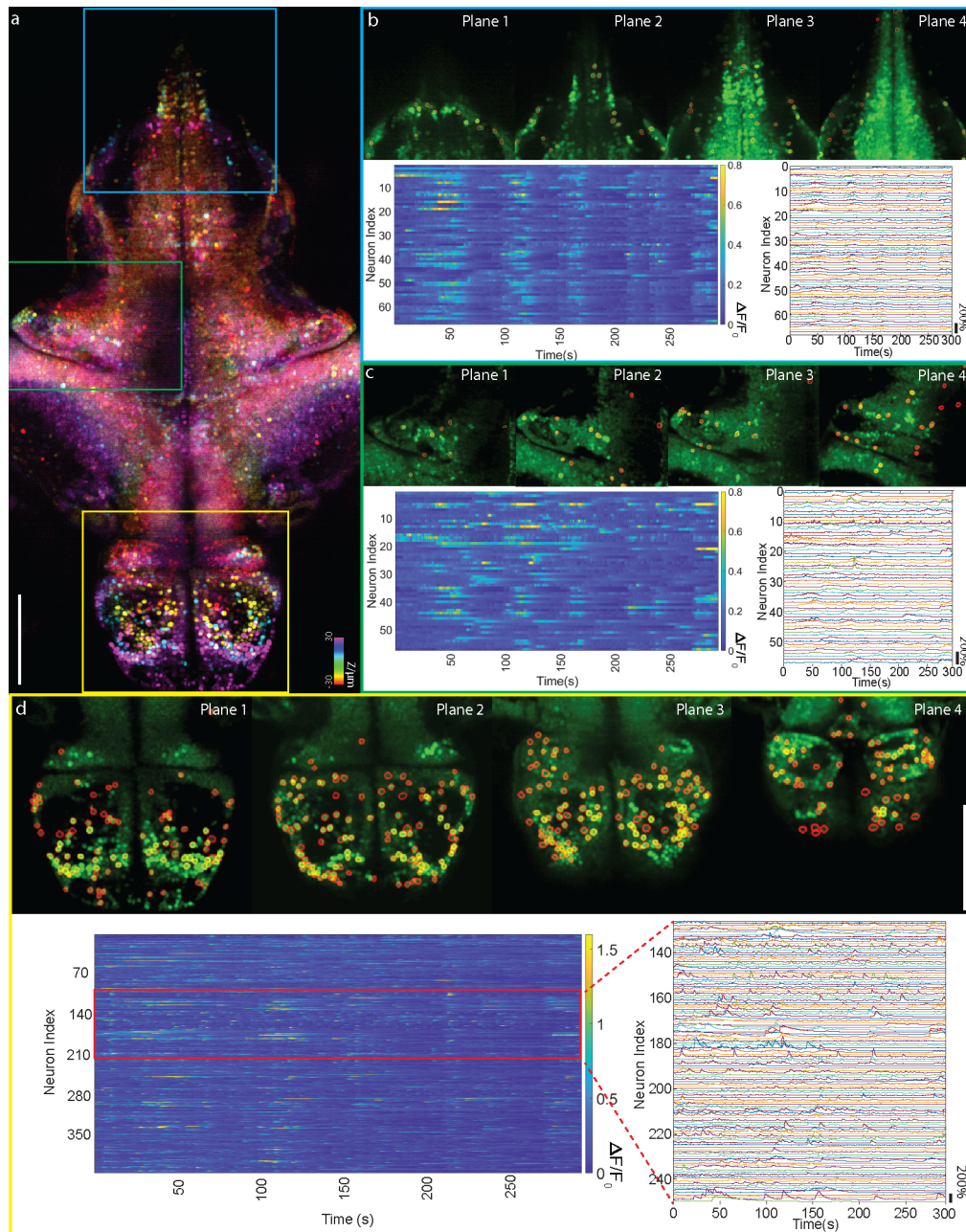
Fig. 7. *In-vivo* calcium imaging of zebrafish brain. (a) Merged temporal max-min projection with color corresponding to depth. (b)-(d) Expanded views of the brainstem, optic tectum-cerebellum, and telencephalon regions indicated by cyan, green, and yellow ROIs in (a) respectively. Top: max-min projection from separate planes. Bottom: activity of identified neurons. Planes 1-4: deepest to shallowest. Scale bar: 100 μm.

5. Discussion

In summary, we describe a multi-z microscopy technique that provides multiplane, optically sectioned imaging over relatively large FOVs with sub-micron resolution. This enabled us to

image beating sarcomere structures in live hiPSC-CMT samples at $5Hz$ frame rates, as well as calcium dynamics in an adult c. elegans and in the entire brain region of a zebrafish larvae, both at $15Hz$ frame rates. The key difference between our new microscope compared to its original implementation [30] is the addition of a DOE in the illumination path that splits the excitation beam into multiple high-NA foci as opposed to a single low-NA focus. This enabled us to achieve sub-micron resolution on par with conventional confocal microscopes, but with the advantage that multiple planes are imaged simultaneously instead of just a single plane. While this improvement in resolution addresses a primary limitation of our original multi-z implementation, it is noted that it comes with a price, namely, the excitation power is no longer as efficiently utilized in our current setup. That is, rather than recycling the same laser power from plane to plane in our single extended-focus implementation, here roughly only a quarter of the laser power is delivered to each focus. This means that to achieve the same detectability as a conventional confocal microscope, the laser power must be increased by roughly a factor of four, and the sample must be able to tolerate such an increase in power. Of course, intermediate solutions can be easily envisaged where the illumination beam is split into fewer foci that are only partially extended, resulting in a compromise between gain in excitation efficiency versus resolution.

Our resolution improvement is not only lateral but also axial, meaning that the gaps between imaging planes become more pronounced. In the event that filling these gaps becomes desirable, without loss of resolution, a possible solution involves the use of a fast axial scanner such as an electrically tunable lens (ETL) [45], a tunable acoustic gradient (TAG) lens [46], a deformable mirror [4,47], or even a voice coil [48]. The advantage of a multi-z microscope, in this case, is that the stroke of the scanner need only be a fraction of what is required to fill the entire volume, leading to a concomitant increase in volume imaging rate. Indeed, the main advantage of multi-z microscopy is imaging speed. We made no effort in this work to push the speed of our microscope since we were more focused on resolution; however, we previously demonstrated the possibility of near-kilohertz multiplane imaging with multi-z microscopy [31], albeit with a reduced field of view.

We close with a word about the use of a DOE to perform multi-focus imaging. This has been done before using widefield microscopy, where the DOE is placed in the detection path [49,50]. It has been done before in scanning microscopes, where, particularly with the advent of metalens technology [51], the DOE can be used to engineer the excitation focus into essentially arbitrary patterns [27,52–56]. To our knowledge, ours is the first application where multiple excitation and detection foci are conjugated, enabling simultaneous multiplane imaging with all the advantages of confocal imaging, such as high resolution and intrinsic optical sectioning, without any requirement of computational background removal or image reconstruction. While the use of a DOE may seem to limit the possibility of interplane separation adjustment, we have shown that this is not the case with changes in magnification. Indeed, we believe the simplicity and flexibility of multi-z microscopy, now with the capability of high-resolution imaging, should make it attractive as a general usage tool for bioimaging.

Disclosures. The authors declare no competing financial interests.

Data availability. Data presented in this paper are not publicly available at this time but may be obtained from the authors upon reasonable request.

Supplemental document. See Supplement 1 for supporting content.

References

1. T.-L. Liu, S. Upadhyayula, and D. E. Milkie, *et al.*, "Observing the cell in its native state: Imaging subcellular dynamics in multicellular organisms," Science **360**(6386), eaaq1392 (2018).

2. J. Mertz, "Strategies for volumetric imaging with a fluorescence microscope," Optica **6**(10), 1261–1268 (2019).

3. M. Martínez-Corral, P.-Y. Hsieh, A. Doblas, E. Sánchez-Ortiga, G. Saavedra, and Y.-P. Huang, "Fast axial-scanning widefield microscopy with constant magnification and resolution," J. Disp. Technol. **11**(11), 913–920 (2015).

4. W. J. Shain, N. A. Vickers, B. B. Goldberg, T. Bifano, and J. Mertz, "Extended depth-of-field microscopy with a high-speed deformable mirror," Opt. Lett. **42**(5), 995–998 (2017).

5. E. J. Botcherby, R. Juskaitis, M. J. Booth, and T. Wilson, "Aberration-free optical refocusing in high numerical aperture microscopy," Opt. Lett. **32**(14), 2007 (2007).

6. T.-H. Chen, J. Ault, H. A. Stone, and C. B. Arnold, "High-speed axial-scanning wide-field microscopy for volumetric particle tracking velocimetry," Exp. Fluids **58**(5), 41 (2017).

7. K. A. Johnson, D. Noble, R. Machado, T. C. Paul, and G. M. Hagen, "Flexible multiplane structured illumination microscope with a four-camera detector," Photonics **9**(7), 501 (2022).

8. A. Descloux, K. Grußmayer, E. Bostan, T. Lukes, A. Bouwens, A. Sharipov, S. Geissbuehler, A.-L. Mahul-Mellier, H. Lashuel, M. Leutenegger, and T. Lasser, "Combined multi-plane phase retrieval and super-resolution optical fluctuation imaging for 4d cell microscopy," Nat. Photonics **12**(3), 165–172 (2018).

9. S. Abrahamsson, J. Chen, B. Hajj, S. Stallinga, A. Y. Katsov, J. Wisniewski, G. Mizuguchi, P. Soule, F. Mueller, C. D. Darzacq, X. Darzacq, C. Wu, C. I. Bargmann, D. A. Agard, M. Dahan, and M. G. L. Gustafsson, "Fast multicolor 3d imaging using aberration-corrected multifocus microscopy," Nat. Methods **10**(1), 60–63 (2013).

10. B. Hajj, J. Wisniewski, M. El Beheiry, J. Chen, A. Revyakin, C. Wu, and M. Dahan, "Whole-cell, multicolor superresolution imaging using volumetric multifocus microscopy," Proc. Natl. Acad. Sci. **111**(49), 17480–17485 (2014).

11. B. Hajj, M. El Beheiry, and M. Dahan, "Psf engineering in multifocus microscopy for increased depth volumetric imaging," Biomed. Opt. Express **7**(3), 726–731 (2016).

12. L. Sacconi, E. Froner, R. Antolini, M. Taghizadeh, A. Choudhury, and F. Pavone, "Multiphoton multifocal microscopy exploiting a diffractive optical element," Opt. Lett. **28**(20), 1918–1920 (2003).

13. S. Xiao, H. Gritton, H.-a. Tseng, D. Zemel, X. Han, and J. Mertz, "High-contrast multifocus microscopy with a single camera and z-splitter prism," Optica **7**(11), 1477–1486 (2020).

14. F. Ströhl, D. H. Hansen, M. N. Grifo, and Å. B. Birgisdottir, "Multifocus microscopy with optical sectioning and high axial resolution," Optica **9**(11), 1210–1218 (2022).

15. L. Sacconi, L. Silvestri, E. C. Rodríguez, G. A. Armstrong, F. S. Pavone, A. Shrier, and G. Bub, "Khz-rate volumetric voltage imaging of the whole zebrafish heart," Biophys. Rep. **2**(1), 100046 (2022).

16. M. Levoy, R. Ng, A. Adams, M. Footer, and M. Horowitz, "Light field microscopy," in *ACM SIGGRAPH 2006 Papers*, (2006), pp. 924–934.

17. R. Prevedel, Y.-G. Yoon, M. Hoffmann, N. Pak, G. Wetzstein, S. Kato, T. Schrödel, R. Raskar, M. Zimmer, E. S. Boyden, and A. Vaziri, "Simultaneous whole-animal 3d imaging of neuronal activity using light-field microscopy," Nat. Methods **11**(7), 727–730 (2014).

18. G. Massaro, D. Giannella, A. Scagliola, F. D. Lena, G. Scarcelli, A. Garuccio, F. V. Pepe, and M. D'Angelo, "Light-field microscopy with correlated beams for high-resolution volumetric imaging," Sci. Rep. **12**(1), 16823 (2022).

19. N. Wagner, N. Norlin, J. Gierten, G. de Medeiros, B. Balázs, J. Wittbrodt, L. Hufnagel, and R. Prevedel, "Instantaneous isotropic volumetric imaging of fast biological processes," Nat. Methods **16**(6), 497–500 (2019).

20. W. J. Shain, N. A. Vickers, A. Negash, T. Bifano, A. Sentenac, and J. Mertz, "Dual fluorescence-absorption deconvolution applied to extended-depth-of-field microscopy," Opt. Lett. **42**(20), 4183–4186 (2017).

21. P. Wu, D. Zhang, J. Yuan, S. Zeng, H. Gong, Q. Luo, and X. Yang, "Large depth-of-field fluorescence microscopy based on deep learning supported by fresnel incoherent correlation holography," Opt. Express **30**(4), 5177–5191 (2022).

22. C. Xiao, Z. Smith, and K. Chu, "Simultaneous recovery of both bright and dim structures from noisy fluorescence microscopy images using a modified tv constraint," J. Microsc. **275**(1), 24–35 (2019).

23. Y. Wu, Y. Rivenson, H. Wang, Y. Luo, E. Ben-David, L. A. Bentolila, C. Pritz, and A. Ozcan, "Three-dimensional virtual refocusing of fluorescence microscopy images using deep learning," Nat. Methods **16**(12), 1323–1331 (2019).

24. Y.-X. Ren, J. Wu, Q. T. Lai, H. M. Lai, D. M. Siu, W. Wu, K. K. Wong, and K. K. Tsia, "Parallelized volumetric fluorescence microscopy with a reconfigurable coded incoherent light-sheet array," Light: Sci. Appl. **9**(1), 8 (2020).

25. Z. Jiao, Z. Zhou, Z. Chen, J. Xie, Y. Mu, J. Du, and L. Fu, "Simultaneous multi-plane imaging light-sheet fluorescence microscopy for simultaneously acquiring neuronal activity at varying depths," Optica **10**(2), 239–247 (2023).

26. B. Chen, X. Huang, D. Gou, J. Zeng, G. Chen, M. Pang, Y. Hu, Z. Zhao, Y. Zhang, Z. Zhou, H. Wu, H. Cheng, Z. Zhang, C. Xu, Y. Li, L. Chen, and A. Wang, "Rapid volumetric imaging with bessel-beam three-photon microscopy," Biomed. Opt. Express **9**(4), 1992–2000 (2018).

27. W. Chen, Q. Zhang, R. Natan, J. Fan, and N. Ji, "Bessel-droplet foci enable high-resolution and high-contrast volumetric imaging of synapses and circulation in the brain in vivo," bioRxiv, 2022.03.05.483143 (2022).

28. D. R. Beaulieu, I. G. Davison, K. Kılıç, T. G. Bifano, and J. Mertz, "Simultaneous multiplane imaging with reverberation two-photon microscopy," Nat. Methods **17**(3), 283–286 (2020).

29. J. Demas, J. Manley, F. Tejera, K. Barber, H. Kim, F. M. Traub, B. Chen, and A. Vaziri, "High-speed, cortex-wide volumetric recording of neuroactivity at cellular resolution using light beads microscopy," Nat. Methods **18**(9), 1103–1111 (2021).

30. A. Badon, S. Bensussen, H. J. Gritton, M. R. Awal, C. V. Gabel, X. Han, and J. Mertz, "Video-rate large-scale imaging with multi-z confocal microscopy," Optica **6**(4), 389–395 (2019).

31. T. D. Weber, M. V. Moya, J. Mertz, and M. N. Economo, "High-speed, multi-z confocal microscopy for voltage imaging in densely labeled neuronal populations," bioRxiv, 2021.12.10.472140 (2021).

32. J.-M. Tsang, H. J. Gritton, S. L. Das, T. D. Weber, C. S. Chen, X. Han, and J. Mertz, "Fast, multiplane line-scan confocal microscopy using axially distributed slits," Biomed. Opt. Express **12**(3), 1339–1350 (2021).

33. S. Lindek and E. H. Stelzer, "Confocal theta microscopy and 4pi-confocal theta microscopy," in *Three-dimensional microscopy: image acquisition and processing*, vol. 2184 (SPIE, 1994), pp. 188–194.

34. T. A. Pologruto, B. L. Sabatini, and K. Svoboda, "Scanimage: flexible software for operating laser scanning microscopes," Biomed. Eng. Online **2**(1), 13 (2003).

35. X. Gan and C. Sheppard, "Detectability: a new criterion for evaluation of the confocal microscope," Scanning **15**(4), 187–192 (1993).

36. J. Pawley, *Handbook of biological confocal microscopy*, vol. 236 (Springer Science & Business Media, 2006).

37. J. Javor, J. K. Ewoldt, P. E. Cloonan, A. Chopra, R. J. Luu, G. Freychet, M. Zhernenkov, K. Ludwig, J. G. Seidman, C. E. Seidman, C. S. Chen, and D. J. Bishop, "Probing the subcellular nanostructure of engineered human cardiomyocytes in 3d tissue," Microsystems & Nanoeng. **7**(1), 10 (2021).

38. C. N. Toepfer, A. C. Garfinkel, and G. Venturini, *et al.*, "Myosin sequestration regulates sarcomere function, cardiomyocyte energetics, and metabolism, informing the pathogenesis of hypertrophic cardiomyopathy," Circulation **141**(10), 828–842 (2020).

39. X. Lian, J. Zhang, S. M. Azarin, K. Zhu, L. B. Hazeltine, X. Bao, C. Hsiao, T. J. Kamp, and S. P. Palecek, "Directed cardiomyocyte differentiation from human pluripotent stem cells by modulating wnt/β-catenin signaling under fully defined conditions," Nat. Protoc. **8**(1), 162–175 (2013).

40. J. Javor, S. Sundaram, C. Chen, and D. J. Bishop, "Controlled strain of cardiac microtissue via magnetic actuation," in *2020 IEEE 33rd International Conference on Micro Electro Mechanical Systems (MEMS)*, (IEEE, 2020), pp. 452–455.

41. A. Dubbs, J. Guevara, and R. Yuste, "moco: Fast motion correction for calcium imaging," Front. Neuroinform. **10**, 6 (2016).

42. E. A. Pnevmatikakis, D. Soudry, Y. Gao, T. A. Machado, J. Merel, D. Pfau, T. Reardon, Y. Mu, C. Lacefield, W. Yang, M. Ahrens, R. Bruno, T. M. Jessell, D. S. Peterka, R. Yuste, and L. Paninski, "Simultaneous denoising, deconvolution, and demixing of calcium imaging data," Neuron **89**(2), 285–299 (2016).

43. P. A. Gorski, C. Kho, and J. G. Oh, "Measuring cardiomyocyte contractility and calcium handling in vitro," in *Experimental Models of Cardiovascular Diseases*, (Springer, 2018), pp. 93–104.

44. K. A. Clark, A. S. McElhinny, M. C. Beckerle, and C. C. Gregorio, "Striated muscle cytoarchitecture: an intricate web of form and function," Annu. Rev. Cell Dev. Biol. **18**(1), 637–706 (2002).

45. K. D. Mac, M. M. Qureshi, M. Na, S. Chang, T. J. Eom, H. S. Je, Y. R. Kim, H.-S. Kwon, and E. Chung, "Fast volumetric imaging with line-scan confocal microscopy by electrically tunable lens at resonant frequency," Opt. Express **30**(11), 19152–19164 (2022).

46. M. Duocastella, G. Vicidomini, and A. Diaspro, "Simultaneous multiplane confocal microscopy using acoustic tunable lenses," Opt. Express **22**(16), 19293–19301 (2014).

47. M. Zurauskas, M. Frade, and M. Booth, "Deformable mirror based remote focusing for fast three-dimensional microscopy," in *Three-Dimensional and Multidimensional Microscopy: Image Acquisition and Processing XXIII*, vol. 9713 (SPIE, 2016), pp. 180–184.

48. P. Rupprecht, A. Prendergast, C. Wyart, and R. W. Friedrich, "Remote z-scanning with a macroscopic voice coil motor for fast 3d multiphoton laser scanning microscopy," Biomed. Opt. Express **7**(5), 1656 (2016).

49. S. Banerji, M. Meem, A. Majumder, B. Sensale-Rodriguez, and R. Menon, "Extreme-depth-of-focus imaging with a flat lens," Optica **7**(3), 214–217 (2020).

50. J. Greene, Y. Xue, J. Alido, A. Matlock, G. Hu, K. Kiliç, I. Davison, and L. Tian, "Edof-miniscope: pupil engineering for extended depth-of-field imaging in a fluorescence miniscope," bioRxiv, 2022.08.05.502947 (2022).

51. W. T. Chen, A. Y. Zhu, V. Sanjeev, M. Khorasaninejad, Z. Shi, E. Lee, and F. Capasso, "A broadband achromatic metalens for focusing and imaging in the visible," Nat. Nanotechnol. **13**(3), 220–226 (2018).

52. A. Chong, W. H. Renninger, D. N. Christodoulides, and F. W. Wise, "Airy–bessel wave packets as versatile linear light bullets," Nat. Photonics **4**(2), 103–106 (2010).

53. S. R. P. Pavani and R. Piestun, "Three dimensional tracking of fluorescent microparticles using a photon-limited double-helix response system," Opt. Express **16**(26), 22048–22057 (2008).

54. C. Roider, A. Jesacher, S. Bernet, and M. Ritsch-Marte, "Axial super-localisation using rotating point spread functions shaped by polarisation-dependent phase modulation," Opt. Express **22**(4), 4029–4037 (2014).

55. L. von Diezmann, Y. Shechtman, and W. Moerner, "Three-dimensional localization of single molecules for super-resolution imaging and single-particle tracking," Chem. Rev. **117**(11), 7244–7275 (2017).

56. L. Gao, L. Shao, B.-C. Chen, and E. Betzig, "3d live fluorescence imaging of cellular dynamics using bessel beam plane illumination microscopy," Nat. Protoc. **9**(5), 1083–1101 (2014).